Nanoscale Horizons

The home for rapid reports of exceptional significance in nanoscience and nanotechnology

Accepted Manuscript

Published on 13 July 2026

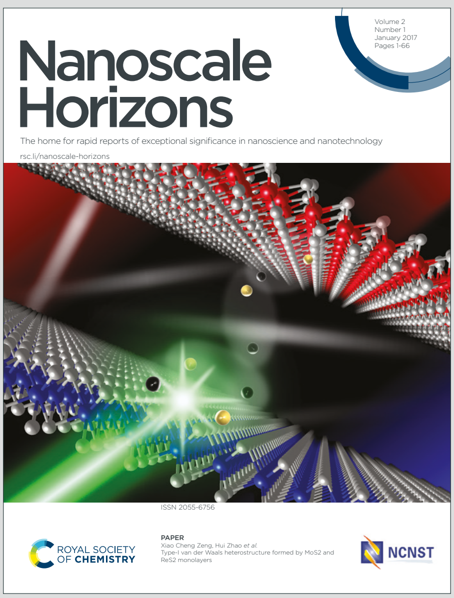

ROYAL SOCIETY OF CHEMISTRY

rsc.li/nanoscale-horizons

New Concepts

This work demonstrates that anomalous cryogenic transconductance in nanoscale quasi-ballistic transistors originates from quantum-capacitance-induced electrostatic renormalization, rather than from additional transport nonidealities. In a 65 nm Si transistor measured from 250 K to 12 K, a Landauer-consistent transport model accurately reproduces the drain current but cannot capture the low-temperature transconductance shoulder. By decomposing transconductance into transport and charge-response terms, the study identifies a rapidly varying gate-control factor, governed by quantum capacitance, as the missing physical mechanism. This concept differs from existing transport-centric descriptions because it treats carrier statistics, sub-band occupation, and gate-to-channel charge coupling as primary determinants of differential device response. A compact two-crossover quantum-capacitance framework simultaneously reproduces both drain current and transconductance, including the cryogenic shoulder. The work provides a materials-level insight that the electronic density of states and quantum-statistical charge susceptibility can reshape observable transistor response even when the current itself remains smooth, offering a predictive route for cryogenic CMOS and quantum-interface electronics.

Quantum capacitance-induced transconductance anomalies in cryogenic quasi-ballistic transistors

Dokyoung Lee[1,2], Hyeonsik Ahn[3], Jusung Kim[1,2], Moon-Seok Kim[4*] and Sungho Kim[1,2,*]

[1]Division of Electronic and Semiconductor Engineering, Ewha Womans University, Seoul 03760, Republic of Korea

[2]Institute for Multiscale Matter and Systems (IMMS), Ewha Womans University, Seoul 03760, Republic of Korea

[3]Department of Electronic Engineering, Hanbat National University, Daejeon 34158, Republic of Korea

[4]Department of Semiconductor Convergence, Chungnam National University, Daejeon 34134, Republic of Korea

Corresponding author: Moon-Seok Kim (kimms@cnu.ac.kr) and Sungho Kim (sunghok@ewha.ac.kr)

ABSTRACT

Understanding the transconductance (g_m) at cryogenic temperature remains a major challenge in the physics-based modeling of nanoscale field-effect transistors. Although short-channel drain current (I_D)–gate voltage characteristics can often be described accurately within transport-based formalisms, the corresponding g_m commonly exhibits pronounced low-temperature anomalies that remain unexplained. Here, we investigate a 65-nm Si n-channel transistor measured from 250 K down to 12 K and show that a Landauer-consistent model provides an accurate quasi-ballistic transport baseline for the I_D across the full temperature range, but fails to reproduce the shoulder-like g_m feature that emerges at deep cryogenic temperature. We show that this residual discrepancy originates not from transport nonidealities but from quantum capacitance (C_q)-induced electrostatic renormalization of gate-induced charge modulation. By decomposing the g_m into transport and charge-response contributions, and introducing a gate-control factor governed primarily by the C_q, we derive a compact framework in which the corrected g_m consists of renormalized baseline and differential electrostatic terms. A two-crossover parameterization of C_q in the effective gate-overdrive domain enables simultaneous and self-consistent reproduction of both the I_D and g_m, including the cryogenic shoulder. These results identify anomalous cryogenic g_m as a C_q-induced signature of rapidly varying gate-to-charge coupling in quasi-ballistic transistors.

1. Introduction

The transconductance (g_m) constitutes a fundamental figure of merit that governs the performance of field-effect transistors (FETs) across both device and circuit hierarchies.[1] It directly determines small-signal voltage gain, noise efficiency, and energy-delay trade-offs, and underpins established low-power and low-noise circuit design methodologies that exploit the ratio between g_m and drain current (g_m/I_D).[2–4] A rigorous physical interpretation of g_m is essential for reliable device optimization and circuit-level performance predictability. However, at deep cryogenic temperatures, a systematic discrepancy emerges: although drain current–gate voltage (I_D–V_G) transfer characteristics are often reproduced with reasonable fidelity using conventional transport formalisms, the corresponding g_m exhibits pronounced anomalies, including nonmonotonic behavior, systematic peak shifts, and substantial quantitative deviations from experimental observations.[5–8] These behaviors are reproducible across device ensembles and temperature ranges, but cannot be attributed to numerical differentiation artifacts, parameter-extraction instabilities, or measurement uncertainty. Rather, they point to a fundamental deficiency in the physical description of V_G-mediated current modulation in cryogenic FETs, indicating that the breakdown of g_m predictability reflects an unresolved physical mechanism intrinsic to the cryogenic operating regime.[9–12]

Existing theoretical and compact-modeling frameworks have predominantly interpreted cryogenic FET characteristics from a transport-centric perspective, extending drift-diffusion formalisms and incorporating quasi-ballistic or injection-limited effects via Landauer-type descriptions.[13–17] Such approaches have been successful in capturing the I_D under low-field conditions by accounting for finite channel length, temperature-dependent scattering, and ballistic transmission constraints. However, they implicitly assume that V_G-induced charge modulation remains classical and only weakly temperature-dependent. This assumption becomes increasingly untenable at deep cryogenic temperatures in which the g_m probes not only the carrier transmission efficiency but also the degree to which the V_G modulates the channel electrochemical potential.[15–17] By definition, $g_m = \partial I_D/\partial V_G$ and directly reflects the V_G sensitivity of the inversion charge density. In this regime, the pronounced sharpening of the Fermi–Dirac distribution and emergence of quantum capacitance (C_q) associated with discrete sub-band occupation modify the electrostatic coupling between the gate and channel.[18–20] The gate-control factor governing charge modulation acquires a strong dependence on both the temperature and gate bias, determined by the combined influence of oxide, quantum, interface state, and depletion capacitances. Even when the I_D is accurately captured within transport-based frameworks, the corresponding g_m can deviate substantially unless electrostatics and carrier statistics are treated as primary physical determinants alongside transport phenomena.

Despite these insights, a critical gap persists in existing literature. Prior studies have largely treated transport corrections and electrostatic effects in isolation, without establishing a unified framework that can simultaneously account for both the I_D and g_m at cryogenic temperatures.[9,10,13] In particular, although quantum capacitance, interface states, and related electrostatic contributions have been discussed in the context of charge accumulation or threshold-voltage behavior, their quantitative influence on g_m has rarely been examined in a manner that is self-consistent with transport-limited current flow. The persistent discrepancy between the accurately reproduced I_D and anomalous g_m has often been attributed to phenomenological mobility degradation, parameter-extraction artifacts, or device-specific nonidealities, rather than shortcomings in the underlying physical description.[21] To date, a systematic analysis that explicitly separates the sensitivity of the current to the channel charge from the sensitivity of that charge to the V_G, and clarifies how quantum-statistical electrostatics govern the g_m in the cryogenic regime, has remained absent. This lack of a unified, physics-grounded framework has hindered the coherent interpretation of cryogenic g_m anomalies and limited the predictive capability of existing models.

In this study, we establish a physics-based framework for the g_m analysis in cryogenic FETs. We adopted a Landauer-consistent I_D model as a transport baseline to minimize the ambiguities associated with quasi-ballistic carrier transmission and isolate transport-related contributions to the current. We demonstrate that the persistent inconsistency between accurately reproduced I_D and anomalous g_m originates from gate-induced charge modulation governed by C_q and related electrostatic capacitances, rather than transport nonidealities. The temperature- and bias-dependent evolution of the C_q was quantitatively modeled using Fermi–Dirac statistics, explicitly capturing the effects of sub-band occupancy and sharpening of carrier distribution at deep cryogenic temperatures. By incorporating these quantum-statistical electrostatic effects into the gate-control factor, we developed a physically consistent g_m model that enables the simultaneous and self-consistent reproduction of both the I_D and g_m across the cryogenic regime. This framework elucidates the physical origin of cryogenic g_m anomalies and provides a predictive basis for interpreting and modeling g_m beyond transport-centric descriptions.

2. Landauer-Consistent Drain Current Model and Transconductance Anomaly

2.1 Temperature-dependent transfer characteristics and anomalous g_m behavior at deep cryogenic temperatures

Figure 1 presents the temperature-dependent transfer characteristics of the Si n-FET investigated in this study (see Methods), featuring a physical gate length and channel width of L = 65 nm and W = 2 μm, respectively. Measurements were performed over a wide temperature range from 250 K down to 12 K at a fixed drain bias of $V_D = 0.1$ V. As the temperature decreased, the transfer characteristics exhibited systematic and well-known trends, including an enhanced subthreshold slope and increased on-state I_D at a given V_G. These changes reflect reduced phonon scattering and the consequent improvement in carrier transport efficiency at cryogenic temperatures.[22,23] Despite the pronounced temperature dependence, the overall shape of transfer characteristics remained smooth and monotonic over the entire temperature range. No abrupt features or anomalous structures were observed in the I_D itself, even at the lowest temperature of 12 K.

In contrast, the corresponding g_m characteristics, shown in Fig. 1b, display a qualitatively different temperature dependence. At elevated temperatures (T ≥ 75 K), the g_m exhibited a single, well-defined peak as a function of the V_G, consistent with conventional expectations based on smooth gate-induced charge modulation. As the temperature decreased, this peak systematically shifted toward higher V_G and increased in magnitude, indicating enhanced gate control and reduced thermal smearing. However, at a deep cryogenic temperature (T = 12 K), the g_m departs from this monotonic evolution. In addition to the primary g_m peak, a distinct shoulder-like feature emerges on the higher-V_G side of the main peak. This shoulder feature is reproducible across multiple measurements and devices and is absent at higher temperatures, indicating that it is an intrinsic characteristic of operation in the deep cryogenic regime rather than an experimental artifact or numerical differentiation effect. Importantly, no corresponding feature was observed in the transfer characteristics, demonstrating that the anomaly manifested exclusively in the g_m. The coexistence of a smooth I_D and nontrivial structure in g_m highlights the qualitative difference between the V_G dependence of the I_D and g_m at deep cryogenic temperatures to motivate a more detailed examination of the underlying physical origin in the following sections.

2.2 Landauer-consistent transport baseline

The device investigated in this work has a physical gate length of L = 65 nm, for which finite channel length effects become appreciable, particularly under cryogenic operation where the carrier mean free path increases as phonon scattering is suppressed. Under such conditions, the low-field I_D can no longer be interpreted solely within a purely diffusive drift–diffusion picture. In the conventional linear-regime description, the I_D is written as

$$I_D = \frac{W}{L}\mu_{app}C_{ox}V_{Gt}V_D\,, \qquad V_{Gt} = V_G - V_T - \frac{V_D}{2}\,, \tag{1}$$

where C_{ox} is the oxide capacitance per unit area, V_T is the threshold voltage, V_{Gt} denotes the effective gate overdrive, and μ_{app} denotes the apparent mobility inferred from electrical measurements. To account phenomenologically for the reduction in mobility with increasing inversion level, μ_{app} is commonly parameterized as

$$\mu_{app}(V_{Gt}) = \frac{\mu_0}{1+\theta_1 V_{Gt} + \theta_2\left(V_{Gt} - \Delta V_T\right)^2}\,, \tag{2}$$

where μ_0 is the low-field mobility, and θ_1, θ_2, and ΔV_T are phenomenological parameters describing field-dependent mobility attenuation. Although this formulation is adequate in the diffusive limit, the mobility extracted from the measured I_D–V_G characteristics in a short-channel device no longer represents a purely scattering-limited quantity once the quasi-ballistic injection becomes non-negligible. Instead, it incorporates both the channel scattering and injection constraint imposed by the finite channel length.

To establish a physically consistent transport baseline, we adopted the Landauer-consistent I_D model that we previously developed and published for the quasi-ballistic transport analysis of short-channel FETs.[21] In the present study, this model was not re-derived in the main text; only its essential form is summarized, while the derivation is provided in Supplementary Notes 1 and 2. Within that framework, the phenomenological mobility attenuation is reinterpreted as the effective, scattering-limited mobility, while the experimentally inferred apparent mobility is decomposed into scattering-limited and ballistic contributions through a Matthiessen-like relation.[24,25] This leads to the compact linear-regime I_D expression:

$$I_D = \frac{W}{L} C_{ox} V_D \frac{\mu_0 V_{Gt}}{F(V_{Gt}) + \eta}, \tag{3}$$

with

$$F(V_{Gt}) = 1 + \theta_1 V_{Gt} + \theta_1 (V_{Gt} - \Delta V_T)^2, \qquad \eta = \frac{\mu_0}{\mu_{ball}}. \tag{4}$$

Here, $F(V_{Gt})$ captures the V_G-dependent attenuation associated with scattering within the channel, while η represents the gate bias-independent injection-limited constraint arising from the finite channel length. Because these two terms originate from distinct physical mechanisms, they cannot be absorbed into a single effective attenuation function. Importantly, η does not introduce an additional independent fitting parameter because the ballistic mobility μ_{ball} is determined by the channel length and temperature within the Landauer formalism; thus, the adjustable mobility-related parameters remain identical to those of the conventional drift–diffusion model. The quantitative advantage of this formulation was established in our previous work over the temperature range of 12−250 K,[21] where the conventional drift–diffusion model exhibited systematic deviations in the low-temperature, high-V_G regime and yielded nonphysical mobility-attenuation parameters, whereas the Landauer-consistent model improved the reproduction of the measured I_D without increasing the number of adjustable mobility-related fitting parameters. Therefore, in the present work, the Landauer-consistent formulation is adopted as an already benchmarked quasi-ballistic transport baseline rather than introduced as a new fitting model.

2.3 Experimental manifestation of the residual I_D–g_m inconsistency

Figure 2 compares the experimentally measured transfer characteristics and g_m with the predictions of the Landauer-consistent transport baseline introduced above. The extracted parameters $\{V_T, \mu_0, \theta_1, \theta_2, \text{and } \Delta V_T\}$ are summarized in Table S1. As shown in Fig. 2a, the Landauer-consistent model reproduces the measured I_D with high quantitative accuracy over a wide temperature range, from deep cryogenic (T = 12 K) to near room temperature (T = 250 K) conditions. In particular, both the enhancement of the on-state current at low temperature and the smooth, systematic evolution of the transfer characteristics with temperature were accurately captured. This agreement confirms that once quasi-ballistic injection constraints are properly incorporated, the I_D of the proposed short-channel device can be consistently described within a transport-centric framework.

In contrast, the corresponding g_m characteristics exhibited a residual and systematic discrepancy, as shown in Fig. 2b. Although the Landauer-consistent baseline captures the overall temperature evolution of g_m and significantly improved its description compared with a purely diffusive interpretation, deviations persist as the temperature is reduced. Most notably, the shoulder-like feature observed on the higher-V_G side of the primary g_m peak at T = 12 K is not reproduced by the transport baseline, despite the fact that the underlying I_D is accurately captured using the same physically constrained parameter set. This point is crucial: the remaining mismatch cannot be eliminated simply by further adjustment of transport parameters because those parameters are already constrained by the successful reproduction of the I_D. The residual discrepancy indicates that even after the dominant quasi-ballistic transport contribution is accounted for, an additional physical mechanism remains necessary to describe the V_G dependence of the g_m in the deep cryogenic regime.

This residual inconsistency cannot be ascribed to numerical differentiation noise or limited measurement resolution because the anomalous g_m feature is reproducibly observed in repeated measurements. The coexistence of an accurately reproduced I_D and incompletely described g_m also shows that a quantitatively successful transport model does not guarantee a correct description of the corresponding g_m. While the I_D primarily reflects the magnitude of the current transport, the g_m probes the sensitivity of that current to the V_G-induced charge modulation. Therefore, the residual cryogenic g_m anomaly points to missing physics not in the overall transport baseline, but in how the channel charge responds to the gate bias. This observation motivated the analysis developed in the following sections, in which the origin of the anomaly is traced to quantum-statistical electrostatics governing gate-induced charge modulation.

3. Transconductance Decomposition and Quantum-Statistical Charge Modulation

3.1 Formal decomposition of transconductance

To elucidate the physical origin of the residual cryogenic g_m anomaly identified in Section 2.3, it is useful to explicitly separate the roles of transport and charge modulation in the g_m. By definition, $g_m = dI_D/dV_G$. In the linear regime, the I_D may be regarded as a function of the channel charge, while the channel charge itself depends on the channel electrochemical potential μ, which is in turn controlled by the applied gate bias. Applying the chain rule yields

$$g_m = \frac{dI_D}{dQ_{ch}} \frac{dQ_{ch}}{d\mu} \frac{d\mu}{dV_G}, \tag{5}$$

where Q_{ch} is the inversion charge per unit area in the channel. Equation (5) provides a physically transparent decomposition of the g_m into three distinct factors. The first factor, dI_D/dQ_{ch}, represents the transport efficiency with which the channel charge contributes to current flow. The second factor, $dQ_{ch}/d\mu$, quantifies the susceptibility of the inversion charge to shifts in the channel electrochemical potential and is governed by carrier statistics. The third factor, $d\mu/dV_G$, describes how effectively the applied V_G modulates the channel electrochemical potential through the gate-stack electrostatics.

Within the present framework, the transport-related factor dI_D/dQ_{ch} was already constrained by the successful reproduction of the measured I_D using the Landauer-consistent transport baseline introduced in Section 2.2. Therefore, the unresolved issue is not the overall magnitude of the current transport itself, but the differential sensitivity of that current to the V_G-induced charge modulation. Equation (5) clarifies why an accurate description of the I_D does not automatically guarantee a correct prediction of the g_m, while the I_D reflects the magnitude of the channel charge weighted by transport efficiency. The g_m probes how sensitively that charge responds to gate bias. The two models yield nearly indistinguishable I_D–V_G characteristics while producing substantially different g_m values if their treatment of electrostatic charge modulation differs. This distinction becomes particularly important in the deep cryogenic regime, where the Fermi–Dirac distribution becomes sharply narrowed, and the channel charge response acquires strong quantum statistical sensitivity. The residual g_m discrepancy identified in Section 2.3 is most naturally associated with the charge-modulation part of Eq. (5), rather than with a further refinement of the transport baseline itself.

3.2 Quantum statistical origin of charge susceptibility

At deep cryogenic temperatures, the gate-induced modulation of channel charge can no longer be described by a purely classical approximation, such as $\partial Q_{ch}/\partial V_G \approx C_{ox}$. As thermal broadening is suppressed, charge accumulation becomes governed by the energy-resolved occupation of quantized sub-band states rather than by a continuous classical capacitance response. Under strong vertical confinement in the inversion layer, the carrier system may be approximated as a quasi-two-dimensional electron gas with sub-band quantized motion normal to the interface.[26] In this regime, the inversion-layer sheet density is expressed as

$$n_s = \sum_n \int_{E_n}^{\infty} D_{2D,n}(E) f(E-\mu) dE, \tag{6}$$

where $f(E-\mu)$ is the Fermi–Dirac distribution and E_n is the edge of the n^{th} sub-band. For each sub-band, the two-dimensional density of states is given by

$$D_{2D,n}(E) = D_{2D}\Theta(E-E_n), \qquad D_{2D} = \frac{g_s g_v m^*}{2\pi\hbar^2}, \tag{7}$$

where Θ denotes the Heaviside step function, and g_s, g_v, and m^* denote the spin degeneracy, valley degeneracy, and in-plane transport effective mass, respectively.

The inversion charge per unit area is $Q_{ch} = -qn_s$. The susceptibility of the channel charge to shifts in the electrochemical potential was quantified using the quantum capacitance C_q. Defining C_q as a positive quantity,

$$C_q \equiv q^2 \frac{\partial n_s}{\partial \mu} = -\frac{\partial Q_{ch}}{\partial \mu}, \tag{8}$$

and differentiating Eq. (6) with respect to μ yields

$$C_q = q^2 \sum_n \int_{E_n}^{\infty} D_{2D,n}(E)\left(-\frac{\partial f(E-\mu)}{\partial E}\right) dE. \tag{9}$$

Equation (9) shows that the C_q is governed by the convolution of the density of states with the derivative kernel $-\partial f/\partial E$, which is centered around $E = \mu$ and has a characteristic width in the order of k_BT. For a constant two-dimensional density of states within each sub-band, Eq. (9) simplifies to

$$C_q = q^2 D_{2D} \sum_n f(\mu - E_n). \tag{10}$$

Equation (10) shows that the C_q is directly proportional to the occupation probability of each sub-band edge. As the electrochemical potential approached a sub-band minimum E_n, the corresponding contribution to C_q evolves from 0 to q^2D_{2D} over an energy window set by thermal broadening. At finite temperature, this is a smooth crossover rather than a discontinuity. However, as the temperature decreased, the crossover width contracts approximately in proportion to k_BT, and the slope $dC_q/d\mu$ correspondingly increased.

This quantum statistical sharpening affects the I_D and g_m in fundamentally different ways. In this study, the I_D is described using the Landauer-consistent transport baseline in Section 2.2. The underlying charge accumulation remains governed by the energy integral in Eq. (6), which evolves smoothly with the gate bias even when the electrochemical potential approaches a sub-band edge.

In contrast, the C_q depends on the derivative of the occupation function, and amplifies the local sensitivity to energy alignment. As thermal broadening collapses, C_q acquires a strongly bias-dependent variation with respect to μ, even though the measured transfer characteristics remain smooth and monotonic. The role of C_q established in this study is to quantify the intrinsic susceptibility of the inversion charge to shifts in the electrochemical potential of the channel. The conversion of this susceptibility into an experimentally observable V_G response requires the additional electrostatic relation between V_G and μ, which depends on the gate-stack capacitance. Section 4 describes how this quantum-statistical charge susceptibility is translated into an electrostatic renormalization of the Landauer-consistent transport baseline, ultimately yielding the observed cryogenic anomaly in g_m.

4. Quantum Capacitance-Induced Electrostatic Renormalization of the Landauer-Consistent Baseline

4.1 Electrostatic renormalization of the Landauer-consistent baseline

Section 2 established the Landauer-consistent model as the transport baseline for the present short-channel device. Section 3 showed that the residual cryogenic g_m anomaly originates not from the transport factor itself but from the V_G sensitivity of the channel charge. This section incorporates the electrostatic limitation of the gate-induced charge modulation into the established transport baseline.

In the linear regime, the I_D is proportional to the mobile charge induced in the channel. Within the Landauer-consistent baseline introduced in Section 2.2, this charge modulation is treated implicitly through the effective gate overdrive, such that the resulting current $I_{D,0}$ corresponds to the reference case, in which gate control is transferred efficiently to the channel. In other words, the baseline current already contains the transport constraint associated with quasi-ballistic injection, but it does not include the additional reduction in the gate-induced charge modulation caused by the finite semiconductor-side capacitance. Once this finite semiconductor-side charge response is considered, the gate-induced channel charge is no longer determined solely by the oxide capacitance C_{ox}. Instead, only a reduced fraction of the baseline charge effectively contributes to current modulation. Since the linear-regime current is proportional to the channel charge, this reduction can be represented, to the first order, by introducing a gate-control factor $\gamma(V_G,T)$, defined as the ratio between the actual gate-induced mobile charge and the corresponding baseline charge. The electrostatically renormalized current is written as

$$I_{D,new} = \gamma \cdot I_{D,0}\,. \tag{11}$$

Here, γ is not introduced as an empirical fitting coefficient but as a compact representation of the extent to which the gate-induced channel charge is reduced relative to the baseline description. In the classical limit, the semiconductor-side charge response is sufficiently large and does not hinder gate control, $\gamma \rightarrow 1$, and the original Landauer-consistent baseline is recovered. In contrast, in the cryogenic regime, where the semiconductor-side capacitance can become small and strongly bias-dependent owing to quantum-statistical effects, γ may deviate significantly from unity and acquire a pronounced dependence on both V_G and T.

Differentiating Eq. (11) with respect to V_G gives the g_m of the renormalized model as

$$g_{m,new} = \frac{dI_{D,new}}{dV_G} = \gamma g_{m,0} + I_{D,0}\frac{d\gamma}{dV_G}, \tag{12}$$

where $g_{m,0} = dI_{D,0}/dV_G$ is the g_m of the Landauer-consistent baseline. Equation (12) shows that electrostatic renormalization results in two physically distinct contributions. The first term, $\gamma g_{m,0}$, represents the baseline g_m reduced by the finite gate-control factor. The second term, $I_{D,0}(d\gamma/dV_G)$, is a purely differential electrostatic contribution arising from the gate-bias dependence of the gate-control factor itself. This second term becomes particularly important when the semiconductor-side capacitance changes rapidly with the gate bias because under such conditions, even a smooth baseline current can produce a highly nontrivial differential response in the g_m.

This observation is central to the present study. The measured I_D remains smooth and monotonic even at deep cryogenic temperature, indicating that the overall transport baseline is well captured by the Landauer-consistent model. However, the g_m, being a derivative quantity, is much more sensitive to rapid bias-dependent changes in gate control. A strong variation in γ can generate shoulder-like or shifted features in the g_m even when no corresponding anomaly is directly visible in the I_D. The remaining task is to determine how γ is set by the gate-stack electrostatics. In particular, it is necessary to identify how the finite semiconductor-side capacitance reduces the effective gate-to-charge coupling relative to the baseline oxide-controlled limit. This is developed in the following subsection.

4.2 Electrostatic origin of the gate-control factor

Section 4.1 introduced the gate-control factor γ as the ratio between the actual gate-induced mobile charge and the corresponding baseline charge. The remaining task is to determine this factor from the gate-stack electrostatics. Under quasi-static small-signal conditions, an infinitesimal V_G change (dV_G) is not entirely transferred to the channel charge. Instead, it is partitioned between the oxide and finite semiconductor-side charge response such that the actual gate-induced charge modulation is reduced relative to the oxide-controlled baseline limit.

Let V_{ch} denote the channel electrostatic potential and dQ_s denote the differential semiconductor-side charge per unit area induced by an infinitesimal V_G variation. Charge continuity across the gate stack requires

$$dQ_s = C_{ox}(dV_G - dV_{ch}), \tag{13}$$

where C_{ox} is the oxide capacitance per unit area. On the semiconductor side, the same differential charge is related to the channel-potential variation through

$$dQ_s = C_s \cdot dV_{ch}, \qquad C_s = C_q + C_{it} + C_{dep}, \tag{14}$$

where C_q, C_{it}, and C_{dep} denote the quantum, interface state, and depletion capacitances, respectively. Eliminating dV_{ch} from Eqs. (13) and (14) gives

$$\frac{dQ_s}{dV_G} = \frac{C_{ox}C_s}{C_{ox}+C_s} \equiv C_{eff}. \tag{15}$$

Equation (15) shows that the actual incremental gate-to-charge coupling is not C_{ox} but the series-combined effective capacitance C_{eff}. This result clarifies the physical meaning of the renormalization factor introduced in Section 4.1. In the baseline current model, the gate-induced mobile charge is treated implicitly as if the V_G were converted into the channel charge with oxide-limited efficiency, i.e., $dQ_{s,0}/dV_G \approx C_{ox}$. However, when the finite semiconductor-side response is considered, the actual charge modulation is reduced to $dQ_s/dV_G = C_{eff}$. Because the linear-regime I_D is proportional to the mobile channel charge, the ratio between the actual and baseline current responses is given by the corresponding ratio of gate-to-charge coupling factors. The gate-control factor follows naturally as

$$\gamma \equiv \frac{dQ_s / dV_G}{dQ_{s,0} / dV_G} = \frac{C_{eff}}{C_{ox}} = \frac{C_s}{C_{ox} + C_s}. \tag{16}$$

Thus, γ is not an empirical scaling coefficient but the direct electrostatic consequence of series capacitance partitioning between the oxide and semiconductor. In the classical limit $C_s >> C_{ox}$, one obtains $\gamma \rightarrow 1$, such that the original Landauer-consistent baseline is recovered. In contrast, when C_s becomes comparable to or smaller than C_{ox}, the induced channel charge is reduced relative to the baseline oxide-controlled limit, and the current is correspondingly renormalized.

In the most general case, C_s contains contributions from the quantum, interface state, and depletion responses. However, Section 3 showed that the most pronounced cryogenic sensitivity originates from the quantum-statistical evolution of C_q, whose variation with the channel electrochemical potential becomes strongly sharpened as thermal broadening collapses. The minimal working approximation adopted in the present study is to regard the cryogenic anomaly as being dominated, to the first order, by the C_q contribution, such that $C_s \approx C_q$ (see details in Supplementary Note 3). Under this approximation, the gate-control factor reduces to

$$\gamma \approx \frac{C_q}{C_{ox} + C_q}. \tag{17}$$

Equation (17) provides the central bridge between the quantum-statistical charge susceptibility derived in Section 3 and the electrostatically renormalized current and g_m model introduced in Section 4.1. Once C_q is specified, γ follows directly, and the renormalized expressions for I_D and g_m can be evaluated accordingly.

4.3 Practical parameterization of C_q and final analytical model for g_m

Section 3 established that the C_q is governed by the occupation of sub-band edges through the relation $C_q \sim \sum_n f(\mu - E_n)$, where each contribution evolves from zero to a finite value as the channel electrochemical potential approaches the corresponding sub-band minimum. Section 4.2 then established that this C_q directly determines the gate-control factor through $\gamma = C_q/(C_{ox} + C_q)$. To complete the model, it is necessary to express C_q in a form that can be directly evaluated from the measured transfer characteristics.

In principle, one can determine C_q by solving self-consistently for the relation between the channel electrochemical potential μ and applied V_G, and then substituting the resulting $\mu(V_G)$ into the Fermi–Dirac form derived in Section 3. However, such a procedure would require full electrostatic treatment beyond the compact modeling scope of the present study. Because our objective is to construct a physics-grounded analytical model on top of the already established Landauer-consistent transport baseline, we introduced a practical parameterization of C_q in the effective gate-overdrive domain $V_{Gt} = V_G - V_T - V_D/2$, which is the natural independent variable of the baseline current model introduced in Section 2.2.

Under this interpretation, the onset of each sub-band contribution is mapped onto an effective crossover voltage $V_{c,n}$, which represents the value of V_{Gt} at which the corresponding sub-band begins to contribute appreciably to the C_q. The ideal Fermi–Dirac occupation step in the energy domain is then represented in the V_{Gt} domain by a broadened logistic function:

$$f_n(V_{Gt}) = \frac{1}{1+\exp\left(-\dfrac{V_{Gt}-V_{c,n}}{\delta_n}\right)}, \tag{18}$$

where δ_n denotes the effective transition width of the n^{th} crossover in the V_{Gt} domain. This parameter should not be interpreted as a microscopic broadening energy or as a direct measure of disorder/inhomogeneity broadening. Instead, δ_n represents the voltage-domain width of the experimentally observed crossover after the underlying sub-band occupation process is mapped onto the effective gate-overdrive axis. Therefore, it can reflect the combined effects of thermal smearing, electrostatic gate-to-channel conversion, disorder/inhomogeneity broadening, overlap between neighboring crossover components, and other nonidealities that smooth the ideal sub-band turn-on in the experimental data. Using this crossover function, the C_q contribution of the n^{th} sub-band is written as

$$C_{q,n}(V_{Gt})=C^{*}_{q,n}f_n(V_{Gt}), \tag{19}$$

where $C^{*}_{q,n}$ is the amplitude associated with the n^{th} sub-band. For the cryogenic g_m anomaly considered in this study, a single crossover is generally insufficient to reproduce the experimentally observed shoulder-like features on the high-V_G side of the main g_m peak (this is discussed in detail in Section 5.4). Therefore, we adopted a two-crossover parameterization in the minimal working form:

$$C_q(V_{Gt})=C^{*}_{q,1}f_1(V_{Gt})+C^{*}_{q,2}f_2(V_{Gt}) \tag{20}$$

with

$$f_n(V_{Gt})=\frac{1}{1+\exp\left(-\dfrac{V_{Gt}-V_{c,n}}{\delta_n}\right)}, \qquad n=1,2 \tag{21}$$

This form preserves the physical picture established in Section 3, namely, that the C_q increases in a step-like manner as the channel electrochemical potential sequentially approaches distinct sub-band edges, while allowing each transition to be broadened in an experimentally realistic manner. Within this framework, the first crossover primarily governs the main increase in C_q, while the second introduces an additional change in the differential response that can generate a shoulder-like structure in the g_m. To avoid redundant temperature-wise freedom, the amplitudes $C^{*}_{q,1}$ and $C^{*}_{q,2}$ were treated as global parameters shared across all temperatures. The crossover voltages ($V_{c,1}$ and $V_{c,2}$) and widths (δ_1 and δ_2) were allowed to vary within constrained bounds.

With the two-crossover parameterization of Eq. (20), the remaining task is to evaluate the differential electrostatic term introduced in the renormalized g_m expression. Since $V_{Gt} = V_G - V_T -$

$V_D/2$, one has $d/dV_G = d/dV_{Gt}$ for fixed V_T and V_D. The derivative of the gate-control factor is obtained by differentiating the electrostatic relation established in Section 4.2, which yields

$$\frac{d\gamma}{dV_G} = \frac{C_{ox}}{(C_{ox}+C_q)^2}\frac{dC_q}{dV_G}. \tag{22}$$

Accordingly, the structure of the electrostatic correction is determined entirely by the gate-bias dependence of C_q. For the two-crossover form of Eq. (20), the derivative of the C_q is

$$\frac{dC_q}{dV_G} = \sum_{n=1}^{2} C^*_{q,n}\frac{df_n}{dV_G}. \tag{23}$$

Using Eq. (21), each crossover function satisfies

$$\frac{df_n}{dV_G} = \frac{df_n}{dV_{Gt}} = \frac{1}{\delta_n} f_n(V_{Gt})\left[1 - f_n(V_{Gt})\right],\ n = 1,2 \tag{24}$$

so that Eq. (23) becomes

$$\frac{dC_q}{dV_G} = \sum_{n=1}^{2}\frac{C^*_{q,n}}{\delta_n} f_n(V_{Gt})\left[1 - f_n(V_{Gt})\right] \tag{25}$$

Substituting Eqs. (22) and (25) into the renormalized g_m expression, Eq. (12) completes the final analytical form of the proposed model. The resulting electrostatic correction is governed by the functions $f_n(V_{Gt})[1 - f_n(V_{Gt})]$, which are localized around $V_{Gt} \approx V_{c,n}$. Consequently, the correction becomes strongly enhanced near the effective crossover voltages associated with sub-band turn-on. This provides a natural mechanism by which a smooth baseline current can generate a nonmonotonic or shoulder-like structure in the g_m. Within this framework, the detailed shape of the cryogenic g_m anomaly is determined by the amplitudes $C^*_{q,n}$, crossover voltages $V_{c,n}$, and transition widths δ_n, which together control the magnitude, position, and sharpness of the electrostatic correction.

5. Results and Physical Interpretation of Quantum Capacitance-Induced Transconductance Renormalization

5.1 Simultaneous reproduction of I_D and g_m by the C_q-corrected model

Figure 3 compares the measured characteristics with the C_q-corrected model (the extracted parameters are summarized in Table S2). The corrected model preserves the high quantitative accuracy of the Landauer-consistent baseline for I_D over the full V_G range considered, from T = 12 K to T = 250 K, as shown in Fig. 3a. The electrostatic renormalization does not degrade the transport description already established for the I_D. Instead, it modifies the gate-to-charge conversion while retaining the smooth and monotonic evolution of the transfer characteristics. In contrast, the improvement becomes evident in the g_m. As shown in Fig. 3b, the same model reproduced the measured g_m with substantially improved accuracy, including the shoulder-like feature observed at 12 K on the higher-V_G side of the main peak. This behavior is not captured by the Landauer-consistent baseline alone. The C_q-corrected framework reproduces not only the magnitude of current transport but also its V_G sensitivity.

Figure 3c shows that this improvement is systematic across temperatures. The mean relative error (MRE) of the I_D remained low, confirming that the electrostatic correction preserved the baseline transport accuracy, while the MRE of the g_m was consistently reduced relative to the Landauer-consistent model. The full multitemperature comparison in Fig. S1 confirms the same trend over all measured temperatures. Taken together, these results show that the missing ingredient in the baseline description is not an additional transport correction but the finite and bias-dependent gate-control factor associated with C_q-induced electrostatic renormalization.

5.2 Differential electrostatic origin of the cryogenic g_m anomaly

The physical origin of the improvement can be identified from the decomposition of the g_m. In Eq. (12), $g_{m,0}$ is the Landauer-consistent baseline g_m such that $\gamma g_{m,0}$ is the multiplicatively renormalized baseline response. $I_{D,0}(d\gamma/dV_G)$ is the differential electrostatic correction. Figure 4a resolves the measured g_m at T = 12 K into these two contributions. A key result is that $\gamma_{gm,0}$ alone does not reproduce the measured cryogenic profile. Although it retains the overall scale and broad shape of the baseline response, it does not generate the shoulder-like feature on the higher-V_G side of the main peak. That feature emerges only when the second term, $I_{D,0}(d\gamma/dV_G)$, is included. The cryogenic anomaly is not produced by a change in the transport backbone itself, but by the gate-bias dependence of the gate-control factor.

The same decomposition remains valid at higher temperatures, but with a much weaker differential contribution. Figure S2 shows that at T = 250 K, the term $I_{D,0}(d\gamma/dV_G)$ is broader and less pronounced, such that the g_m retains a conventional single-peak profile. The contrast between 12 K and 250 K is not a change in mechanism, but a change in the magnitude and localization of the differential electrostatic term. This point also explains why the anomaly is prominent in the g_m

but not in the I_D. The I_D reflects the integrated charge response and remains smooth as long as the charge accumulation evolves continuously with the gate bias. In contrast, $g_m = dI_D/dV_G$ selectively amplifies regions where the gate-control efficiency changes rapidly. Therefore, the cryogenic shoulder is a differential electrostatic feature rather than a transport anomaly.

5.3 Temperature evolution of C_q, γ, and $d\gamma/dV_G$

The origin of the differential correction is clarified by the temperature dependence of C_q, γ, and $d\gamma/dV_G$, as shown in Fig. 4b. At 12 K, the evolution of C_q with the gate bias was relatively steeper than that at 250 K. This behavior follows directly from the suppression of thermal broadening: as the Fermi–Dirac distribution narrows, the crossover in C_q occurs over a smaller V_G interval. At higher temperature, the same crossover is more broadly smeared, and C_q evolves more gradually. Because $\gamma = C_q/(C_{ox} + C_q)$, this sharpening is transferred directly to the gate-control factor. At 250 K, γ varies gradually with V_G, consistent with a relatively smooth gate-to-charge conversion. However, at 12 K, γ changes much more abruptly, indicating that the electrostatic coupling between gate bias and channel charge becomes strongly bias-dependent in the cryogenic regime.

The decisive quantity is the derivative $d\gamma/dV_G$. At 250 K, it is broad and smooth; therefore, its contribution to the g_m is distributed over a wide voltage range and does not create an additional structure. At 12 K, $d\gamma/dV_G$ becomes more localized and more structured, so that the term $I_{D,0}(d\gamma/dV_G)$ is no longer a weak correction, but a pronounced contribution capable of reshaping the g_m profile. The low-temperature shoulder in the g_m is the direct differential signature of quantum-statistical sharpening in the gate-control response.

Figure 4b provides the link between the statistical picture developed in Section 3 and the experimentally observed anomaly. The anomaly does not arise from a discontinuity in the channel charge or a qualitative change in the transport law. It arises because the electrostatic susceptibility of the channel charge becomes sharply redistributed in the V_G as thermal broadening collapses. Once this effect is incorporated through the gate-control factor γ, both the temperature evolution of the g_m and the distinctive shoulder at deep cryogenic temperature follow naturally. Consistent with this interpretation, the extracted crossover voltages $V_{c,1}$ and $V_{c,2}$ exhibited only modest temperature dependence (Table S2), indicating that the dominant temperature evolution arises primarily from the sharpening of the electrostatic response rather than large shifts in crossover position.

5.4 Necessity of the two-crossover description for the cryogenic g_m shoulder

The remaining question is whether a single effective crossover in C_q is sufficient to account for the measured cryogenic g_m, or whether a more structured electrostatic response is required. Figure S3 addresses this point by comparing one- and two-crossover parameterizations for the representative T = 12 K case. For the I_D, both parameterizations showed nearly indistinguishable agreement with the experiment. This indicates that the transfer characteristics alone are not sufficiently sensitive to distinguish whether the underlying electrostatic renormalization proceeds through a single smooth crossover or a more structured sequence of transitions. The integrated current can remain well reproduced as long as the overall gate-control reduction is described correctly.

The distinction emerges clearly in the g_m. Figure S3b shows that the one-crossover model captures the overall rise and fall of the g_m, but fails to reproduce the shoulder-like feature on the higher-V_G side of the main peak. In contrast, the two-crossover model reproduced both the principal peak and subsequent shoulder with substantially improved fidelity. This difference follows directly from the structure of the electrostatic correction: a single crossover produces only one dominant localized variation in C_q, and only one principal feature in $d\gamma/dV_G$, while two partially separated crossovers generate a more structured differential response.

The implication is not that individual sub-bands are spectroscopically resolved in the present data, but that the measured cryogenic g_m requires at least two effective crossover components in the V_G evolution of C_q. The two-crossover form is best understood as the minimal compact representation capable of reproducing the experimentally observed differential electrostatic structure. In this sense, it is not an arbitrary increase in fitting flexibility, but the simplest physically grounded description that self-consistently accounts for the cryogenic shoulder.

6. Conclusion

In summary, we established a unified physical framework to resolve the long-standing inconsistency between accurately reproduced I_D and anomalous g_m in cryogenic short-channel transistors. Using a 65-nm Si n-channel transistor as a representative platform, we showed that a Landauer-consistent transport baseline captures the measured I_D with high accuracy from 250 K to 12 K, but remains insufficient to reproduce the shoulder-like g_m feature that develops at deep cryogenic temperature. This result demonstrates that the successful modeling of the current magnitude alone is not sufficient to describe its V_G sensitivity.

By explicitly separating the transport and charge-modulation effects in the g_m, we identified the missing physics as quantum-statistical electrostatics. As the temperature decreased, the sharpening of the Fermi–Dirac distribution caused the C_q to evolve more abruptly with the gate bias, which in turn produced a strongly bias-dependent gate-control factor. The resulting differential term associated with $d\gamma/dV_G$ becomes sufficiently localized at low temperature to reshape the g_m profile and generate the experimentally observed shoulder. The cryogenic g_m anomaly should therefore be understood not as a transport anomaly in the conventional sense, but as a differential electrostatic consequence of rapidly varying gate-to-charge coupling.

Based on this, we developed a compact C_q-corrected model that preserves the established Landauer-consistent transport backbone while incorporating the electrostatic renormalization of gate-induced charge modulation. This framework simultaneously reproduces both the I_D and g_m across temperatures and shows that the low-temperature shoulder requires a two-crossover description of C_q, indicating a structured evolution of the gate-control response with gate bias. The present results clarify why transport-only descriptions remain incomplete even when they accurately reproduce the transfer characteristics. More broadly, they provide a predictive and physically grounded basis for modeling the g_m under cryogenic transistor operation, where transport and electrostatics must be treated self-consistently rather than independently.

The present compact framework is also complementary to ab initio and DFT-based transport approaches.[27,28] While atomistic calculations can provide material-specific inputs such as the density of states, sub-band structure, transmission function, and energy-dependent conductivity, they would refine the microscopic ingredients rather than change the central transconductance decomposition developed here. In this sense, the proposed model provides an experimentally accessible compact counterpart to atomistic transport simulations for analyzing gate-control-limited g_m behavior in low-dimensional and quantum-capacitance-limited transistor platforms.

Methods

Device fabrication. The device analyzed in this study was an n-channel bulk Si transistor fabricated using a commercial 65-nm low-power complementary metal-oxide semiconductor (CMOS) technology provided by TSMC. A low threshold-voltage device option was used. The transistor was formed on a p-type Si substrate using a conventional planar CMOS process. The gate dielectric consisted of thermally grown SiO_2 with a physical thickness of 2.6 nm. The channel width and gate length were W = 2 μm and L = 65 nm, respectively. No post-fabrication treatment or additional process modifications were introduced after foundry fabrication.

The choice of a 65-nm channel length was motivated by the transport regime of interest. At sufficiently high temperatures, the carrier transport in this geometry remained close to the diffusive limit, while cooling increased the carrier mean free path and progressively enhanced the role of finite-length injection effects. The device provides an experimentally suitable platform for examining the crossover from drift diffusion-like transport to quasi-ballistic transport, and for testing whether transport-only descriptions remain sufficient to explain the measured g_m at cryogenic temperatures.

Electrical measurements. Electrical characterization was performed in a closed-cycle cryogenic probe environment under high vacuum. Gate and drain biases were supplied, and the drain current was recorded using a Keysight B2902 source-measure unit. Cooling was provided by a Gifford–McMahon closed-cycle cryostat (Sumitomo RDK-415D). Although the cryostat was capable of reaching lower temperatures, the measurements analyzed in this study were performed over the range from 250 K down to 12 K at a fixed drain bias of $V_D = 0.1$ V. The gate voltage was swept at a rate of 0.09 V/s, and no measurable hysteresis was observed between forward and reverse transfer scans under this measurement condition.

The sample was mounted on an oxygen-free high-conductivity copper holder mechanically anchored to the second-stage cold head. All measurements were performed at a vacuum level of approximately 10^{-6} Torr. The device temperature was monitored using sensors located near the sample position, and each measurement was acquired only after sufficient thermal stabilization was achieved. An electrical connection to the device was established through dedicated cryostat feedthroughs.

Data analysis and fitting. The measured I_D-V_G characteristics were analyzed using a two-step modeling procedure. In the first step, a Landauer-consistent transport baseline was constructed at each temperature to extract the transport parameters {V_T, μ_0, θ_1, θ_2, and ΔV_T} and generate the reference responses $I_{D,0}$ and $g_{m,0}$. In the second step, the residual discrepancy in the g_m was treated within the C_q-corrected framework by introducing a gate-control factor $\gamma = C_q/(C_{ox} + C_q)$ and fitting the measured I_D and g_m simultaneously using a two-crossover parameterization of C_q in the effective gate-overdrive domain.

For the multitemperature fitting of the corrected model, the C_q amplitudes were treated as global parameters shared across temperatures, while the transport parameters and crossover descriptors were optimized as temperature-dependent local parameters within constrained bounds. The final optimization was performed over the full temperature set using a hierarchical fitting strategy designed to preserve the Landauer-consistent transport backbone, while introducing only the electrostatic degrees of freedom required to reproduce the cryogenic g_m anomaly. A detailed description of the fitting workflow, objective function, parameter hierarchy, optimization procedure, and corresponding pseudocode is provided in Supplementary Note 4. The derivation of the Landauer-consistent transport baseline and the justification of the approximation Cs ≈ Cq are given in Supplementary Notes 1–3.

Acknowledgements

This work was supported by National Research Foundation of Korea (NRF) grants funded by the Korean government (MSIT and MOE) (RS-2024-00449412, RS-2025-16063688).

Competing interests

The authors declare no conflict of interest.

Data availability

The data Supplementary the findings of this study are available from the corresponding author upon request.

References

1 F. Silveira, D. Flandre and P. G. A. Jespers, *IEEE J. Solid-State Circuits*, 1996, **31**, 1314–1319.

2 V. Subramanian, B. Parvais, J. Borremans, A. Mercha, D. Linten, P. Wambacq, J. Loo, M. Dehan, N. Collaert, S. Kubicek, R. J. P. Lander, J. C. Hooker, F. N. Cubaynes, S. Donnay, M. Jurczak, G. Groeseneken, W. Sansen and S. Decoutere, in *International Electron Devices Meeting (IEDM)*, 2005, vol. 2005, pp. 898–901.

3 S. K. Mohapatra, K. P. Pradhan, L. Artola and P. K. Sahu, *Mater. Sci. Semicond. Process.*, 2015, **31**, 455–462.

4 L. Barboni, M. Siniscalchi and B. Sensale-Rodriguez, *IEEE Journal of the Electron Devices Society*, 2015, **3**, 208–216.

5 A. G. Nassiopoulos, D. Tsamakis and E. Rocofyllou, *J. Appl. Phys.*, 1990, **68**, 1896–1901.

6 A. Beckers, F. Jazaeri and C. Enz, *IEEE Trans. Electron Devices*, 2020, **67**, 1357–1360.

7 Y. Liu, L. Lang, Y. Chang, Y. Shan, X. Chen and Y. Dong, *IEEE Trans. Electron Devices*, 2021, **68**, 456–463.

8 E. Catapano, M. Casse and G. Ghibaudo, *IEEE Trans. Electron Devices*, 2023, **70**, 4049–4054.

9 Y. Zhang, T. Lu, W. Wang, Y. Zhang, J. Xu, C. Luo and G. Guo, *IEEE Trans. Electron Devices*, 2021, **68**, 4267–4273.

10 W. Manzoor, A. K. Dutta, G. Pahwa, N. Manzoor, C. Hu and Y. Singh Chauhan, *IEEE Trans. Electron Devices*, 2024, **71**, 4510–4516.

11 N. Pandey, D. Basu and S. K. Banerjee, *IEEE Trans. Electron Devices*, 2026, **73**, 2385–2393.

12 H. Bohuslavskyi, A. G. M. Jansen, S. Barraud, V. Barral, M. Cassé, L. Le Guevel, X. Jehl, L. Hutin, B. Bertrand, G. Billiot, G. Pillonnet, F. Arnaud, P. Galy, S. De Franceschi, M. Vinet and M. Sanquer, *IEEE Electron Device Letters*, 2019, **40**, 784–787.

13 S. K. Singh, S. Gupta, R. A. Vega and A. Dixit, *IEEE Electron Device Letters*, 2022, **43**, 689–692.

14 C. Luo, Z. Li, T. T. Lu, J. Xu and G. P. Guo, *Cryogenics*, 2019, **98**, 12–17.

15 A. Beckers, F. Jazaeri, A. Grill, S. Narasimhamoorthy, B. Parvais and C. Enz, *IEEE Journal of the Electron Devices Society*, 2020, **8**, 780–788.

16 A. Beckers, F. Jazaeri and C. Enz, *IEEE Trans. Electron Devices*, 2018, **65**, 3617–3625.

17 E. R. Hsieh, Z. Y. Wang, Y. S. Huang, T. C. Hung, R. Y. Lyu and K. Y. Lee, *IEEE Trans. Electron Devices*, 2022, **69**, 3575–3580.

18 D. L. John, L. C. Castro and D. L. Pulfrey, *J. Appl. Phys.*, 2004, **96**, 5180–5184.

19 T. Fang, A. Konar, H. Xing and D. Jena, *Appl. Phys. Lett.*, 2007, **91**, 092109.

20 N. Ma and D. Jena, *2d Mater.*, 2015, **2**, 015003.

21 D. Lee, M. Cha, H. Ahn, J. Kim and S. Kim, *Nanoscale Horiz.*, 2026, **11**, 1726–1736.

22 G. Pahwa, P. Kushwaha, A. Dasgupta, S. Salahuddin and C. Hu, *IEEE Trans. Electron Devices*, 2021, **68**, 4223–4230.

23 H. C. Han, F. Jazaeri, A. D'Amico, Z. Zhao, S. Lehmann, C. Kretzschmar, E. Charbon and C. Enz, *Solid. State. Electron.*, 2022, **193**, 108296.

24 M. S. Lundstrom and D. A. Antoniadis, *IEEE Trans. Electron Devices*, 2014, **61**, 225–233.

25 D. Antoniadis, *IEEE Trans. Electron Devices*, 2016, **63**, 2650–2656.

26 T. Ando, A. B. Fowler and F. Stern, *Rev. Mod. Phys.*, 1982, **54**, 437.

27 T. Sakhraoui and F. Karlický, *The Journal of Physical Chemistry C*, 2026, **130**, 8854–8863.

28 S. D. Yang, A. Kumar and B. M. Wong, *ACS Appl. Mater. Interfaces*, 2025, **18**, 2149–2161.

Figure captions

Figure 1. Temperature-dependent transfer characteristics of the 65-nm Si n-channel transistor measured from T = 250 K down to 12 K at a fixed drain bias of V_D = 0.1 V. (a) I_D–V_G characteristics showing the systematic enhancement of the subthreshold slope and on-state current with decreasing temperature while preserving a smooth and monotonic gate-voltage dependence. (b) g_m–V_G characteristics showing the evolution of the g_m peak with temperature and the emergence of a distinct shoulder-like feature on the higher-V_G side of the main peak at 12 K. The absence of a corresponding anomaly in I_D indicates that the cryogenic anomaly manifests specifically in the g_m.

Figure 2. Full multitemperature comparison between the measured characteristics and Landauer-consistent transport baseline over the investigated temperature range of 12 K to 250 K. (a) I_D–V_G characteristics and (b) g_m–V_G characteristics. Symbols represent the measurement data, and lines represent the Landauer-consistent model. The model reproduces the measured I_D with high quantitative accuracy across temperatures, capturing the smooth and systematic evolution of the transfer characteristics. In contrast, although it describes the overall temperature dependence of g_m, it fails to reproduce the shoulder-like feature that emerges at deep cryogenic temperature to reveal a residual I_D–g_m inconsistency beyond the transport baseline.

Figure 3. Full multitemperature comparison between the measured characteristics and C_q-corrected model over the investigated temperature range of 12 K to 250 K. (a) I_D–V_G characteristics and (b) g_m–V_G characteristics. Symbols represent the measurement data, and solid lines represent the C_q-corrected model. (c) Mean relative errors of I_D and g_m as a function of temperature, comparing

the Landauer-consistent and C_q-corrected models. The corrected framework preserves the high accuracy of the transport baseline for I_D while substantially improving the reproduction of g_m across the full temperature range, including the cryogenic shoulder feature.

Figure 4. Physical origin of the cryogenic transconductance anomaly in the C_q-corrected framework. (a) Decomposition of the corrected transconductance at T = 12 K into the multiplicatively renormalized baseline term $\gamma g_{m,0}$ and the differential electrostatic term $I_{D,0}(d\gamma/dV_G)$, together with their sum $g_{m,new}$. Symbols represent the measurement data. The comparison shows that the shoulder-like feature on the higher-V_G side of the main g_m peak does not arise from the renormalized transport baseline alone, but emerges only when the differential electrostatic term is included. (b) Temperature dependence of C_q, γ, and $d\gamma/dV_G$ at T = 12 K and 250 K. As the temperature decreases, the evolution of C_q becomes sharper, which leads to a more abrupt variation of γ and a more localized $d\gamma/dV_G$ to produce the pronounced cryogenic shoulder in g_m.

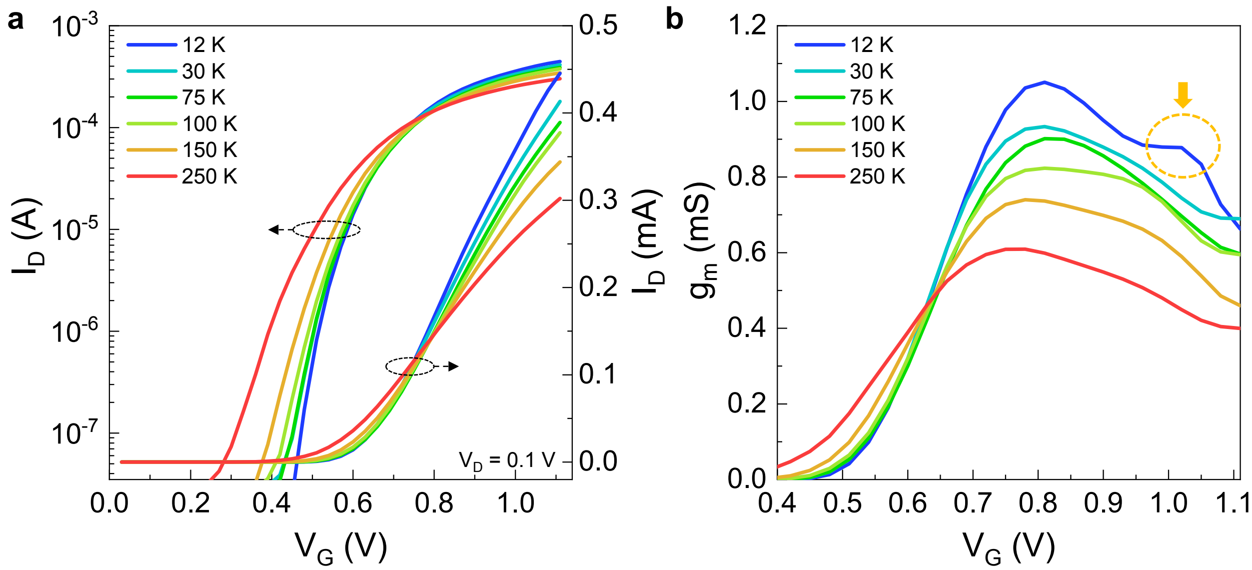
a
b
12 K
30 K
75 K
100 K
150 K
250 K
10^{-3}
10^{-4}
10^{-5}
10^{-6}
10^{-7}
I_D (A)
I_D (mA)
V_D = 0.1 V
V_G (V)
g_m (mS)

Figure 1

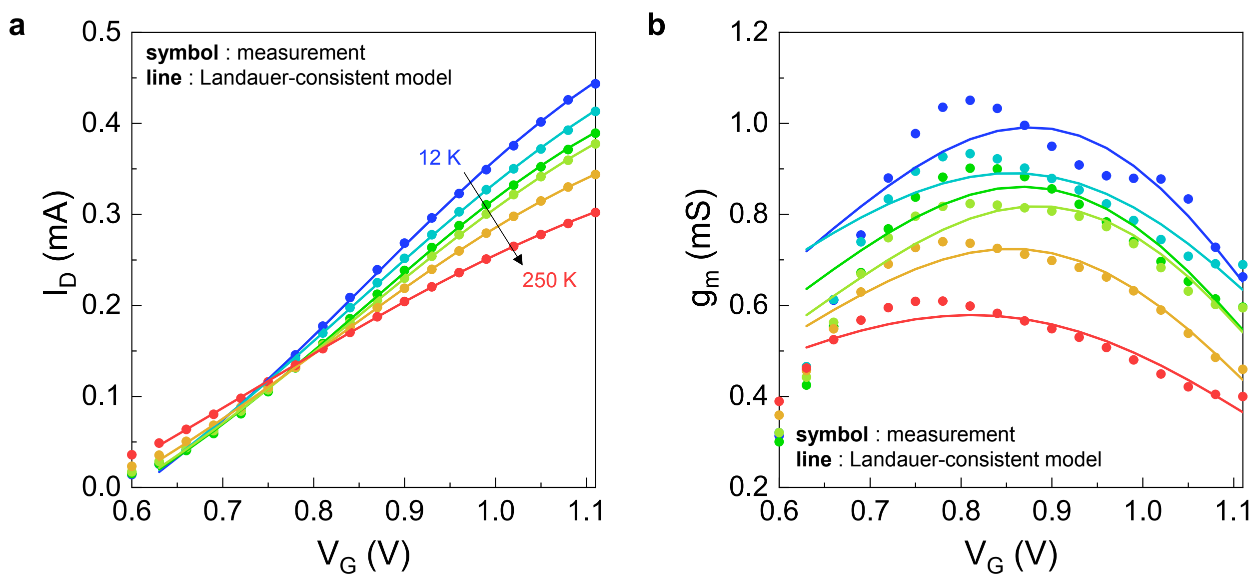
a
symbol : measurement
line : Landauer-consistent model
12 K
250 K
I_D (mA)
V_G (V)
0.0
0.1
0.2
0.3
0.4
0.5
0.6
0.7
0.8
0.9
1.0
1.1
b
symbol : measurement
line : Landauer-consistent model
g_m (mS)
V_G (V)
0.2
0.4
0.6
0.8
1.0
1.2

Figure 2

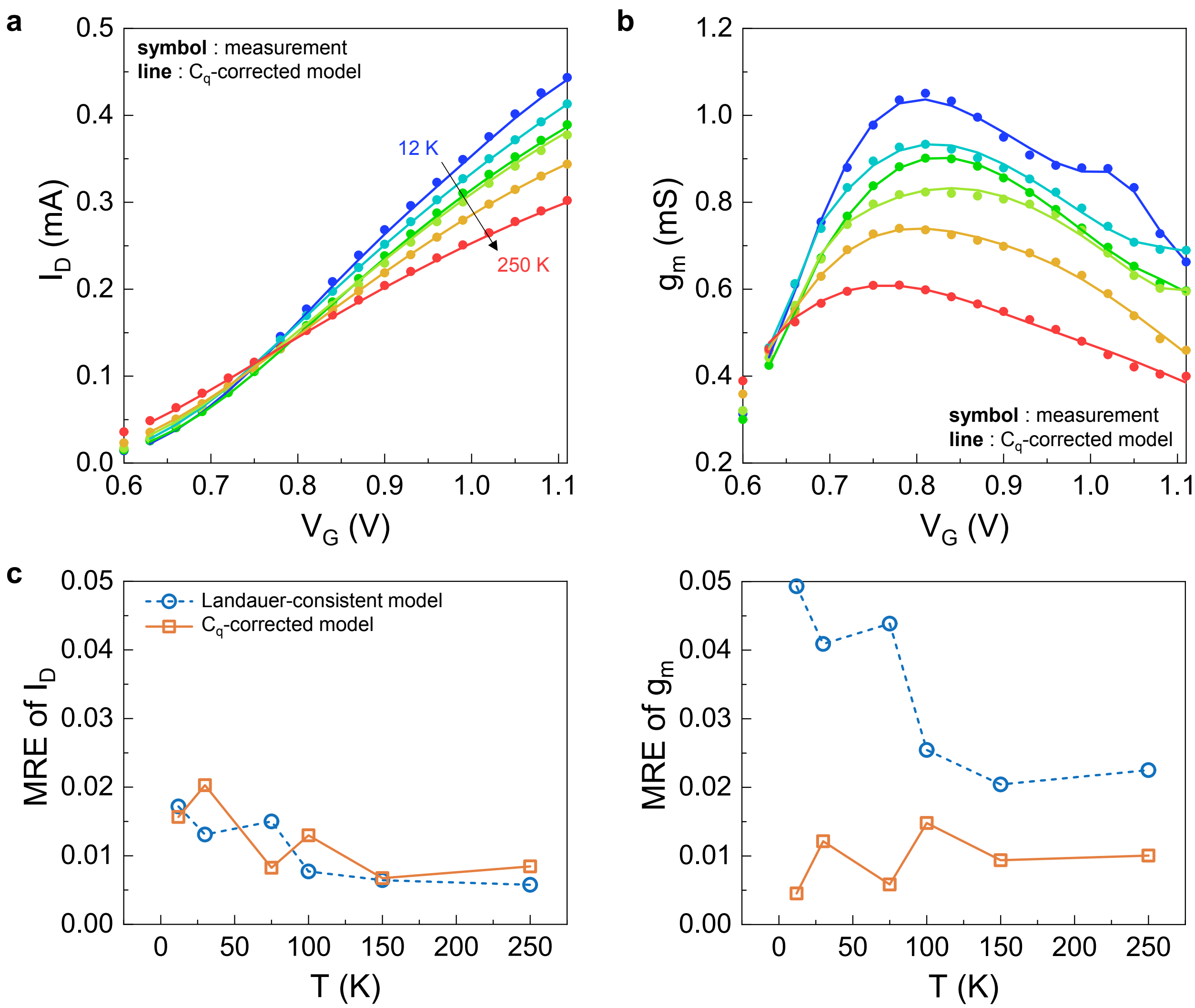
a
b
c
symbol : measurement
line : C_q-corrected model
12 K
250 K
I_D (mA)
g_m (mS)
V_G (V)
Landauer-consistent model
C_q-corrected model
MRE of I_D
MRE of g_m
T (K)

Figure 3

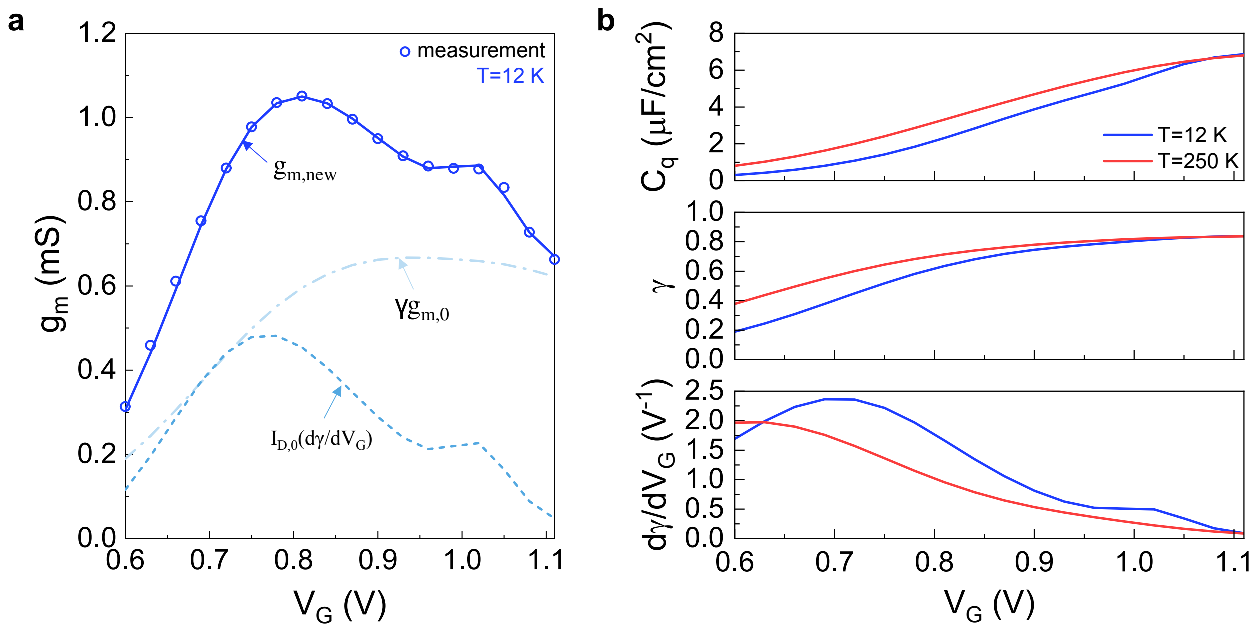
a
b
measurement
T=12 K
$g_{m,new}$
$\gamma g_{m,0}$
$I_{D,0}(d\gamma/dV_G)$
g_m (mS)
V_G (V)
C_q (μF/cm^2)
T=12 K
T=250 K
γ
$d\gamma/dV_G$ (V^{-1})
V_G (V)

Figure 4

Data availability

The data that support the findings of this study, including temperature-dependent electrical measurement data (I_D–V_G and g_m–V_G characteristics) and the processed datasets used for analysis and modeling, are included within the Article and its Supplementary Information. Additional raw data supporting the conclusions of this work are available from the corresponding author upon reasonable request.